Electronic Supplementary Material (ESI) for Chemical Communications.

Photochemically-assisted Fast Abiotic Oxidation of Manganese and Formation of δ–MnO_2 Nanosheets in Nitrate Solution

Haesung Jung, Tandeep S. Chadha, Doyoon Kim, Pratim Biswas, and Young-Shin Jun*

Department of Energy, Environmental and Chemical Engineering, Washington University, St. Louis, Missouri, 63130, United States

E-mail: ysjun@seas.wustl.edu

Phone: (314)935-4539

Fax: (314)935-7211

http://encl.engineering.wustl.edu/

Electronic supplementary information

Table of Contents

Materials and Methods

Supplementary Discussions

1) Confirmation of nitrate photo-excitation by UV light
2) Oxidation state and morphology of the synthesized δ-MnO_2 in natural sunlight
3) Comparison of the abiotic manganese oxidation rate found in this work with those in biotic processes

Supplementary Figures

Supplementary Tables

Supplementary References

Materials and Methods

Solution preparation for experiments. Experiments were conducted at room temperature with 100 μM $Mn(NO_3)_2$ (Alfa Aesar) for up to 6 hrs. To mimic an environmentally relevant pH condition, the initial pH was adjusted to 8.9 ± 0.1 using 0.01 M NaOH (J. T. Baker), and 1 mM $NaNO_3$ (14 ppm (NO_3^-–N); J. T. Baker) was added as the source of nitrate. The nitrate concentration is environmentally relevant based on the USEPA drinking water limit of 0.714 mM (10 ppm (NO_3^-–N)). To avoid any effect from a buffering chemical, we did not use any buffer solution in this study. Thus, pH decreased from 8.9 to 5.3 over 6 hrs (Fig. S10). Because we took samples before Mn oxide aggregation occurred (after 6 hrs, we found that aggregation did occur), we did not conduct experiments for longer than 6 hrs. To analyze the mechanism of manganese oxidation, 0.1 M tert-BuOH (Sigma Aldrich) and 0.5 μM superoxide dismutase (SOD) (Sigma Aldrich) were used to scavenge hydroxyl radicals and superoxide radicals, respectively. To examine the one-electron transfer mechanism, we used 0.5 mM pyrophosphate ($Na_4P_2O_7$, referred as PP) (Sigma Aldrich). The concentration of δ-MnO_2 was quantified using 0.004 % (w/v) leucoberbelin blue (referred as LBB) (Sigma Aldrich). For leucoberbelin blue (LBB) analyses, we used 79% Mn(IV) (2.5 conversion factor) and 21% Mn(III) (5.0 conversion factor) based on our oxidation state value of 3.79+, derived from XPS.[1-3] We used a 1:5 ratio of reacted solution (0.3 ml) and LBB solution (1.5 ml). Therefore, for the background we also used a 1:5 ratio of DI water and LBB.

Photo-oxidation analysis. A 450 W Xe-arc lamp (Oriel) was used as a reliable, controllable light source for the systematic study. The light passed through a 10 cm long IR water filter. The reactor was cylindrical, with a vertical quartz window facing the light source. The reaction solutions were

mixed with a magnetic stirrer. Outdoor natural sunlight exposure tests were also conducted, using opened test tubes placed on the balcony of Whitaker Hall at Washington University (St. Louis, MO, USA, 38.9 °N latitude). The reaction was conducted between 10:30 am and 3:30 pm on July 24th, 2015, in a temperature range from 30 °C to 33 °C.

Solid Phase Characterization. All samples were prepared after the formed particles were washed and centrifuged at 5000 rpm three times. For characterization, we used high-resolution X-ray diffraction, (HRXRD, Bruker D8 ADVANCE X-ray diffractometer with Cu-Kα radiation (λ = 1.5418 Å)) and X-ray absorption spectroscopy (XAS). X-ray photoelectron spectroscopy (XPS, PHI 5000 VersaProbe II, Ulvac-PHI with monochromatic Al Kα radiation (1486.6 eV)) was used to identify the oxidation state of the formed Mn oxide. The C 1s peak (284.8 eV) was taken as the energy reference. We analyzed the shift of the Mn $2p_{3/2}$ spin orbit, the energy gap between Mn $2p_{1/2}$ and the satellite, and the Mn 3s multiplet splitting. For XAS, the Mn K-edge was measured in transmission mode on beamline 13-BM-D at the Advanced Photon Source at Argonne National Laboratory. A Si(111) monochromator, giving a focused beam size of 10 μm by 30 μm and a resolution of 1×10^{-4} ΔE/E, was used to create monochromatic X-rays. The energy flux was 1×10^{9} at 10 keV, and the energy range for this station was 4.5–70 keV. Energy calibration was monitored by using the pre-edge feature of Mn metal foil (6539.0 eV). We used MnO, Mn_2O_3, and δ-MnO_2 provided by beamline 13-BM-D, as the references of Mn(II), Mn(III), and Mn(IV), respectively. In addition, to provide *hk* bands in high resolution, synchrotron-based wide angle X-ray diffraction (WAXD) of the formed particles was performed with an energy of 58.650 keV (λ = 0.2114 Å) on beamline 11-ID-B at the Advanced Photon Source at Argonne National Laboratory. The sample was exposed for 1 s and the measurement was repeated 180 times. The Kapton

background data was also obtained with the same beam exposure time for background subtraction. 1D intensity as a function of d-spacing was obtained by converting the 2D image using Fit2D.[4] An high resolution transmission electron microscope (HRTEM, JEOL 2100F) with a 200 kV accelerating voltage revealed the thickness of the formed Mn oxide. The diluted samples of Mn oxide were placed on a lacey carbon support Cu grid (Ted Pella Inc.). A scanning electron microscope (SEM, FEI Nova NanoSEM 2300) visualized the layered morphology of the formed Mn oxide at a 10kV accelerating voltage. Substrates were coated with Au to increase the conductivity. The working distance was 5−6 mm. The amount of intercalated Na^+ was measured using inductively coupled plasma-mass spectrometer (ICP-MS, Perkin Elmer ELAN DRC II). After the end of the reaction time, to fully remove salt in the solutions, the solutions were centrifuged six times at 5000 rpm. After each centrifugation, the supernatant was pipetted off and discarded, and the precipitate was re-suspended in DI water. The salt-removed samples were dissolved in 10 mM ascorbic acid (Sigma Aldrich), and acidified using 5 ml of 2 % HNO_3 before ICP-MS measurements. NO_2^- concentrations were measured by a Dionex ICS-1600 (Dionex IonPac As22 (4 × 250 mm) column). The surface area and pore size of particles were measured by a NOVA 2200e analyzer (Quantachrome Inc.) after degassing the particles at 110 °C for 24 hrs under vacuum.

Testing the mechanism of fast Mn oxidation and electron transfer. To test the roles of specific ROS on manganese oxidation, we used ROS scavengers and analyzed the subsequent MnO_2 formation colorimetrically with UV-Vis. Leucoberbelin blue (LBB) ($\lambda = 625$ nm, $\varepsilon = 180{,}000\ M^{-1}$) reduces manganese, which has a higher oxidation state than Mn^{2+}.[2] The oxidized LBB in turn displays a blue color, whose intensity is proportional to the concentration of oxidized Mn created by sunlight exposure. Also, to elucidate the electron transfer mechanism, pyrophosphate (PP),

which complexes with Mn(III), was used. The concentration of the Mn(III)-PP complex was analyzed at 258 nm using UV-Vis.

Supplementary Discussions

1) Confirmation of nitrate photo-excitation by UV light

Photochemically-assisted oxidation of Mn and subsequent formation of δ-MnO_2 from Mn^{2+} (aq) occurred through nitrate photolysis. The formation of δ-MnO_2 can be qualitatively observed from the absorption peak of UV-Vis measurement at $\lambda \sim 400$ nm.[5] For this test, to reveal an obvious increase or suppression of the absorption spectrum resulting from the faster formation of δ-MnO_2 at higher nitrate concentration, 100 mM nitrate at initial pH of 8.9 and with 100 μM Mn^{2+} (aq), was used instead of 1 mM nitrate. To confirm the role of UV light in the reaction, a UV filter was installed on the Xe-arc lamp to block UV light ($\lambda < 400$ nm). The UV-Vis absorption spectra of samples with the UV filter ($\lambda > 400$ nm) were the same as for the dark condition (Fig. S4). There was no obvious absorption peak in the UV-Vis spectra under light exposure with the UV filter. On the other hand, obvious absorption peaks in UV-Vis spectra at 400 nm were observed for light exposure without the UV filter, suggesting that the reaction results from UV light, which triggers photolysis of nitrate at a wavelength of ~305 nm.[6, 7] In this study, we tested the effect of hydroxyl radicals and superoxides, which are the most reactive ROS in aqueous systems. We found that superoxide, which is generated from the photolysis of nitrate, is the biggest contributor. We did not test nitrogen oxide radicals because they are known as isolable radicals.[8]

2) Oxidation state and morphology of the synthesized δ-MnO_2 in outdoor natural sunlight

The effect of outdoor sunlight exposure on Mn oxidation and subsequent formation of δ-MnO_2 was investigated. The reaction was conducted between 10:30 am and 3:30 pm on July 24th, 2015, in a temperature range from 30 °C to 33 °C, on the balcony of Whitaker Hall at Washington University (St. Louis, MO, USA, 38.9 °N latitude). Figure S8A shows the sunlight spectrum. The concentration of δ-MnO_2 increased with elapsed time. In the 1 mM nitrate condition, an approximately four times lower concentration was observed in the outdoor sunlight test than in the artificial sunlight experiments (Fig. S8B). The lower intensity of outdoor sunlight at ~305 nm resulted in the lower concentration of δ-MnO_2. However, even in 1 mM nitrate solution, the δ-MnO_2 formation rate is still comparable with that of biotic process. Also, 100 mM nitrate solution promotes fast formation of δ-MnO_2, and can be employed in applications to synthesize δ-MnO_2 in an environmental friendly way. The oxidation state and morphology of the synthesized Mn oxide using outdoor sunlight indicated the formation of δ-MnO_2 as well (Fig. S1).

3) Comparison of the abiotic manganese oxidation rate found in this work with those in biotic processes

Mn oxidation in nature is kinetically-controlled. Without high pH, autocatalysis, and Mn-oxidizing bacteria, the oxidation of Mn^{2+} (aq) takes a very long time.[9, 10] For example, in Diem and Stumm's study, Mn^{2+} (aq) concentration remained at the same level over years in 10 mM nitrate and 20 μM $Mn(NO_3)_2$ at pH 8.4 in the presence of O_2 (P_{O_2} = 0.2 atm).[9] High pH and autocatalysis promote faster oxidation of manganese.[10-13] However, the high pH and autocatalytic conditions showed the oxidation from Mn^{2+} (aq) to Mn(III) only, not to Mn(IV).[10, 11, 13, 14] Photochemical processes are also important for triggering redox reactions in the cycling among Mn(II), Mn(III), and Mn(IV) in

surface water environments.[15-17] A few studies have showed photochemically-induced oxidation with organics.[3, 18] Nico et al. showed the fast oxidation of Mn^{2+} (aq) to Mn(III), and mentioned that Mn(III) was the most dominant oxidation state in their system.[18] Recently, Learman et al. showed the photochemically assisted oxidation of Mn^{2+} (aq) to Mn(IV) with organics in K-medium (2 g/L peptone, 0.5 g/L yeast extract, and 20 mM HEPES buffer) (0.35–0.77 μM/hr).[3] While these studies showed photooxidation with organics, most previous studies focused on the role of light in the reduction of MnO_2.[16, 17, 19-22] The comproportionation-disproportionation process between Mn^{2+} (aq) and initial δ-MnO_2 could change the mineral phase from the initial δ-MnO_2 to Mn(III)OOH or to orthogonal birnessite having up to 33 % Mn(III) in layers.[23-26] Recent studies clarified that it depends on the ratio of Mn^{2+} (aq) to initial δ-MnO_2 and on the pH.[23-25] In any event, the results showed mainly the oxidation of Mn^{2+} (aq) to Mn(III), not to Mn(IV). While comproportionation-disproportionation between Mn^{2+} (aq) and δ-MnO_2 showed a possibility of oxidation to Mn(IV), it was equal exchange between oxidation of Mn^{2+} (aq) to Mn(IV) and reduction of Mn(IV) to Mn^{2+} (aq), not a direct, additional conversion of Mn^{2+} (aq) to Mn(IV).[3, 24] Thus, the comproportionation-disproportionation process between Mn^{2+} (aq) and hexagonal birnessite (δ-MnO_2) is considered an important reductive pathway of Mn redox cycling.[23, 24, 27] On the other hand, because the biotic process showed relatively faster oxidation of Mn^{2+} (aq) to Mn(IV), bacteria-mediated Mn oxidation is believed to be the biggest contributor to the Mn redox reaction, as the oxidative pathway from Mn^{2+} (aq) to Mn(IV) in natural systems. Fast oxidation and the formation of MnO_2 have been observed in the studies of microbial effects on Mn oxidation (e.g., *Bacillus* sp. Strain SG-1,[28] *Leptothrix discophora* strain SS-1[29], *Pseudomonas putida* strains MnB1 and GB-1,[30, 31] marine alphaproteobacterium *Roseobacter* sp. AzwK-3b[2, 32]). The bacterially-mediated formation rates of MnO_2 obtained at the end of reaction or reported values

from previous results are compared in Fig. S9. With the marine alphaproteobacterium, the average of previous formation rates was 0.71 ± 0.35 μM hr^{-1}.[2, 3, 32, 33] Red columns in Fig. S9 are the formation rates of MnO_2 obtained from this study in 1 mM nitrate with sunlight exposure. There is a caveat in this comparison that the approximated δ-MnO_2 formation rates of biotic Mn oxidation were obtained by linearization from zero to the final concentrations at the final times indicated in the previous studies. Because the total reaction times are different due to differences in reaction systems, we compared formation rate, not total yields. Also, because the kinetics of biotic oxidation of Mn(II) are controlled by diverse factors, such as pH, initial Mn(II) concentration, dissolved oxygen, temperature, and the ionic strength of reaction solution, the Mn oxide formation rates in Fig. S9 are good only for relative comparisons, and more systematic studies are required. Contemporary analyses of the kinetics of biotic oxidation under diverse factors were recently done regarding *Bacillus* sp. Strain SG-1.[34] While there are significant changes in the formation rate of MnO_2, most results were between ~0.1 μM hr^{-1} and ~1.4 μM hr^{-1} (spore concentration: 0.7 to 11 × 10^9 spores/L; a pH range: 5.8 to 8.1; temperature: 4 to 58 ºC; dissolved oxygen: 2 to 270 μM; initial Mn(II) concentration: 1 to 200 μM; ionic strength: 0.05 to 0.68).[34] Thus, though different bacteria have different formation rates, the comparable formation rates of our results indicate that photochemically-induced Mn oxidation in nitrate solutions can be a highly possible scenario contributing to δ-MnO_2 formation in the environment, which has not been reported previously. To the best of our knowledge, for the first time, our result shows the fastest oxidation from Mn^{2+} (aq) to Mn(IV) (s), as well as the formation of δ-MnO_2 nanosheets, in an abiotic inorganic system.

Supplementary Figures

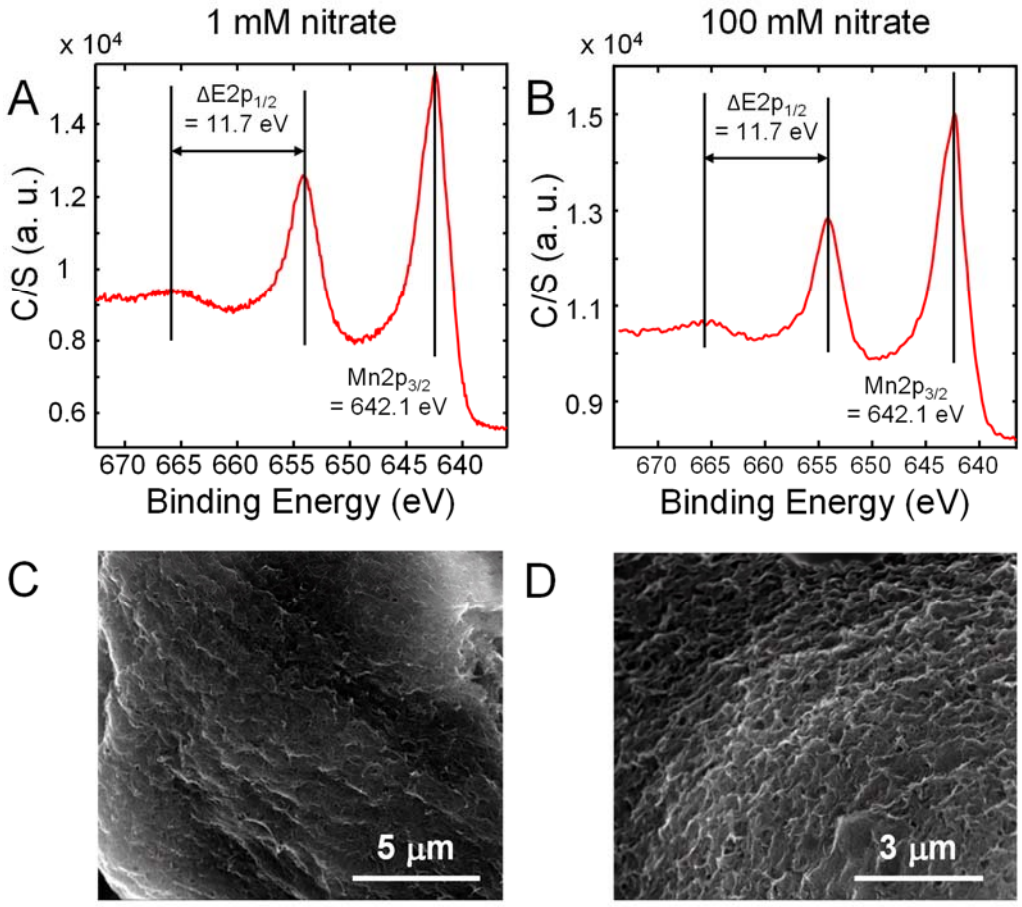

Fig. S1 Characterization of the outdoor sunlight synthesized layered birnessite using Mn2p X-ray photoelectron spectroscopy (XPS) and scanning electron microscopy (SEM). (A) The position of $Mn2p_{3/2}$, and the energy gap between $Mn2p_{1/2}$ and the satellite peak in 1 mM nitrate. (B) The position of $Mn2p_{3/2}$, and the energy gap between $Mn2p_{1/2}$ and the satellite peak in 100 mM nitrate. (C) Layered morphology of the synthesized δ-MnO_2 in 1mM nitrate. (D) Layered morphology of the synthesized δ-MnO_2 in 100 mM nitrate.

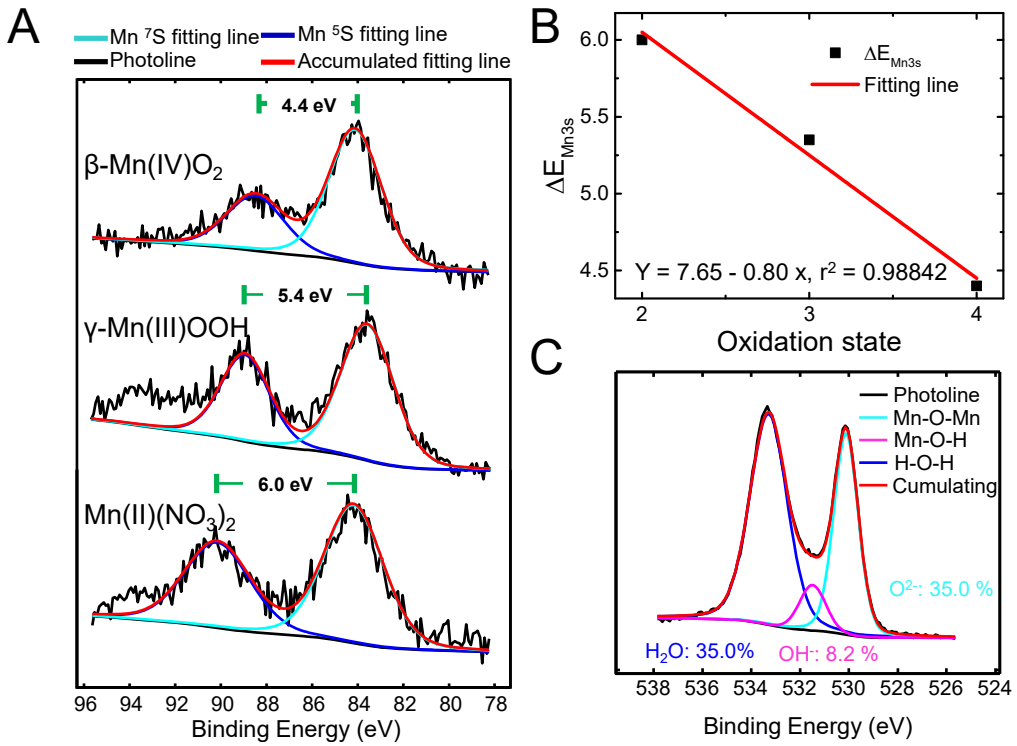

Fig. S2 The determination of oxidation state of the synthesized δ-MnO_2 via XPS specta of Mn 3s and O 1s. (A) Mn 3s photolines of Mn(II) ($Mn(NO_3)_2$, Alpha Aesar), Mn(III) (γ-MnOOH, Mineralogical Research Co.), and Mn(IV) (β-MnO_2, Sigma Aldrich) reference samples indicated Mn 3s multiplet splitting ($\Delta E_{Mn\ 3s}$). (B) Linear fitting of the obtained $\Delta E_{Mn\ 3s}$ indicates that the oxidation state of the synthesized δ-MnO_2 ($\Delta E_{Mn\ 3s}$ = 4.6 eV (Fig. 2B)) is 3.80+.[3, 4] (C) The areas of the deconvoluted O 1s peaks respectively fit the Mn–O–Mn bond for tetravalent oxide (529.8 eV), the Mn–O–H bond for hydrated trivalent oxide (531.5 eV), and the H–O–H bond for residual water (533.3 eV).[1, 2] The fitting of the O 1s spectrum was conducted based on Gaussian-Lorentzian curve-fitting. The obtained areas of the Mn–O–Mn peak and the Mn–O–H peak indicated the oxidation state of the synthesized δ-MnO_2 was 3.77+, $valence = \{IV(area_{Mn-O-Mn} - area_{Mn-O-H}) + III(area_{Mn-O-H})\} / area_{Mn-O-Mn}$.[3] The oxidation states obtained from Mn 3s (3.80+) and O 1s (3.77+) spectra were very similar, so we used an averaged value of 3.79+.

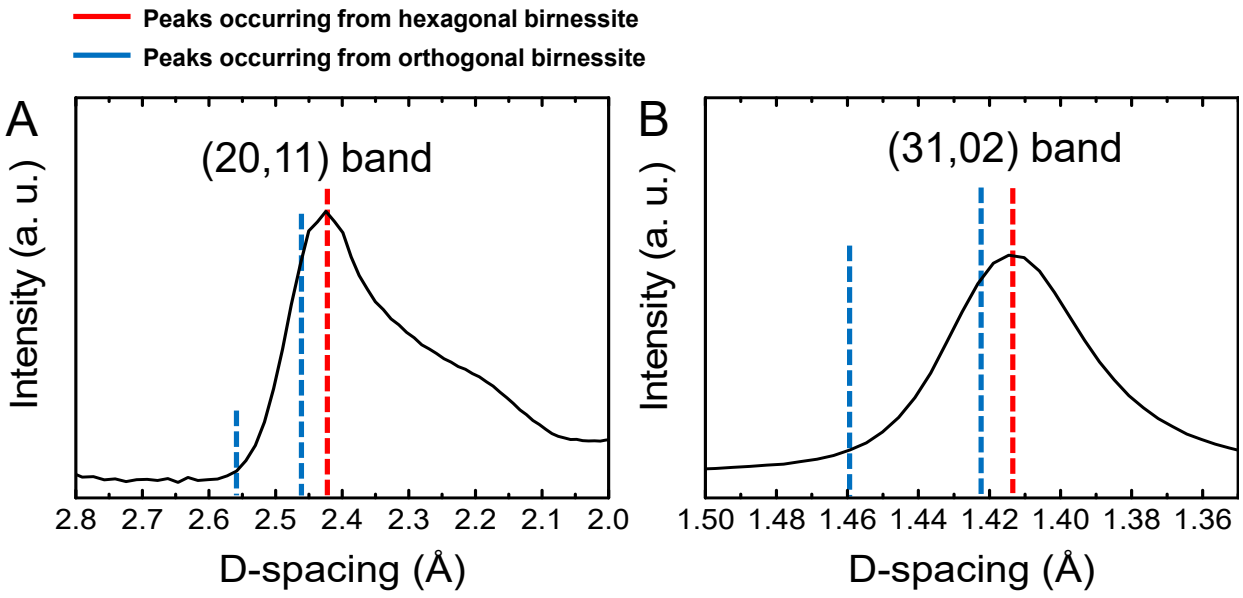

Fig. S3. (20, 11) and (31, 02) bands of the formed particles measured by synchrotron X-ray diffraction. Because c-disordered birnessite has randomly stacked nanosheet structures, (20, 11) and (31, 02) reflections occur as broad *hk* bands, which come from same *hk* reflections and different *l* reflections. c-disordered hexagonal and orthogonal birnessites show differences in peak separation. Peaks at red lines occur from hexagonal birnessite, and peaks at blue lines occur from orthogonal birnessite.[25, 39] The particles show the peaks of hexagonal birnessite without any separation of the peaks. The results confirm that the formed particles are c-disordered hexagonal birnessite (δ-MnO_2), and support the findings of EXAFS.

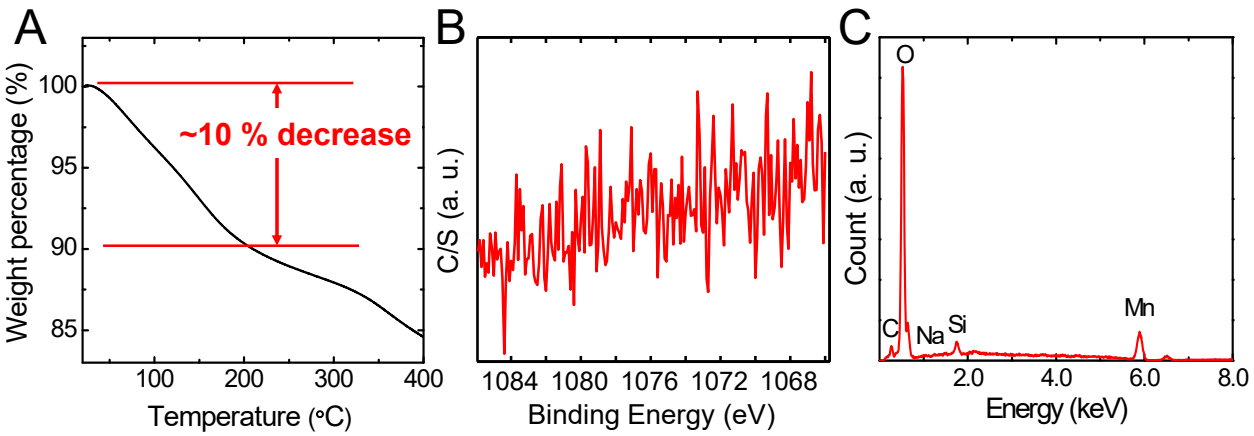

Fig. S4 The amount of water in the synthesized δ-MnO_2 and formation of H^+-birnessite without Na^+ between layers. (A) TGA revealed an ~10 % decrease in the total mass of synthesized δ-MnO_2 below 200 °C, caused by the loss of water. (B) X-ray photoelectron spectroscopy (XPS) spectra did not show a discernible intensity increase at the value of Na 1s binding energy (~ 1072 eV). (C) Energy dispersive spectrometry (EDS) also did not show Na^+.

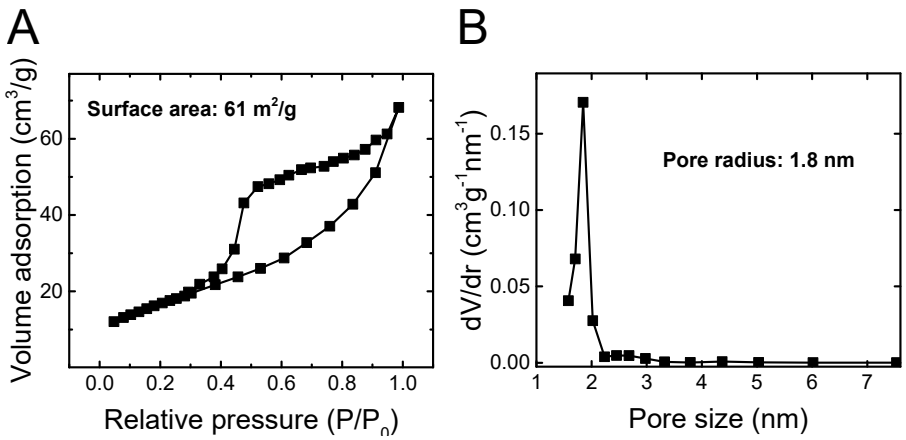

Fig. S5 (A) The nitrogen adsorption/desorption isotherm of δ-MnO_2 nanosheets confirms a surface area of 61 m^2/g. (B) Barett-Joyner-Halenda (BJH) pore size distribution curve shows a peak centered at 1.8 nm.

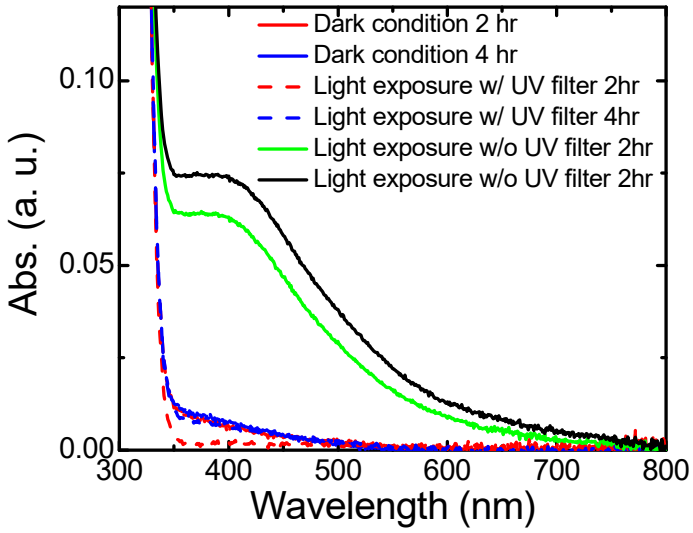

Fig. S6 The effect of light wavelength on manganese oxidation. With a UV filter installed, the filtered light does not promote manganese oxidation and subsequent formation of δ-MnO_2.

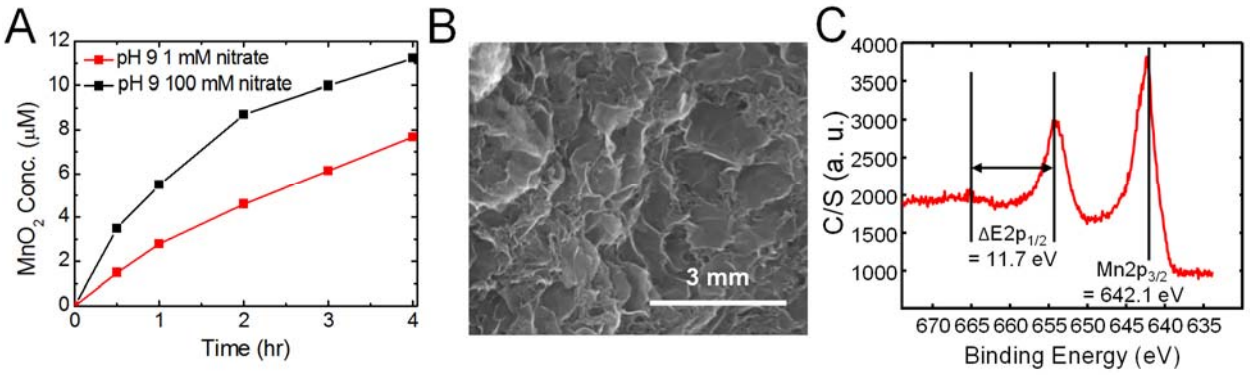

Fig. S7 Photochemically-assisted synthesis of δ-MnO_2 in 100 mM nitrate solution showed faster formation of δ-MnO_2. (A) *In situ* measurements of MnO_2 concentrations under varied nitrate concentrations. (B) Layered morphology of the synthesized δ-MnO_2. (C) Mn 2p XPS spectrum indicating the binding energy of Mn $2p_{3/2}$, 642.1 eV, and the energy gap between Mn $2p_{1/2}$ and the satellite peak, 11.7 eV. Those results indicate the formation of δ-MnO_2.

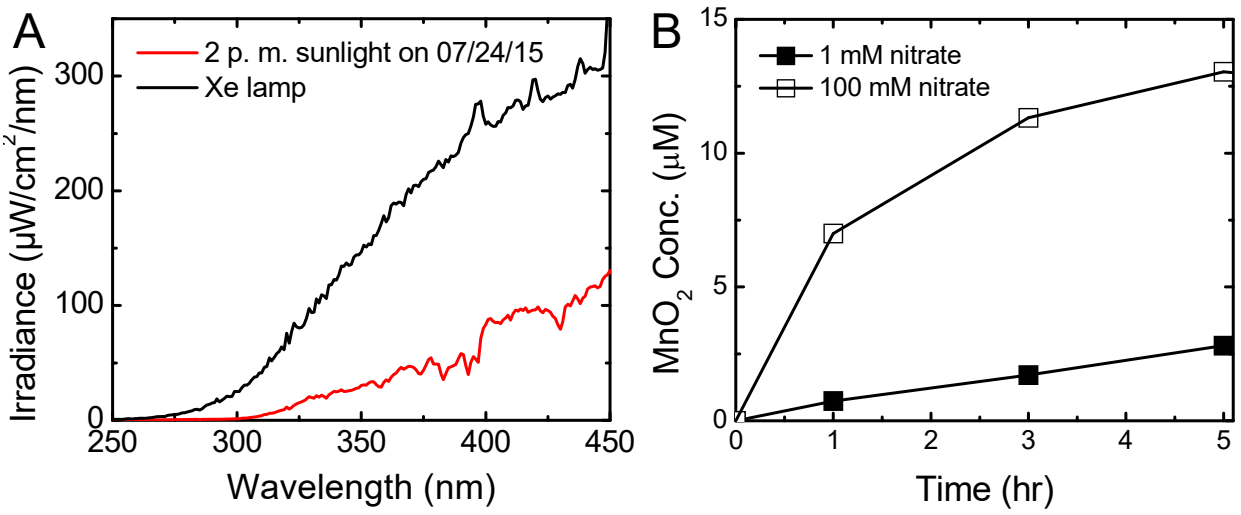

Fig. S8 The formation of δ-MnO_2 in outdoor sunlight. (A) Sunlight spectrum on July 24th of 2015. (B) *In situ* measurement of the δ-MnO_2 concentrations with 1 mM and 100 mM nitrate.

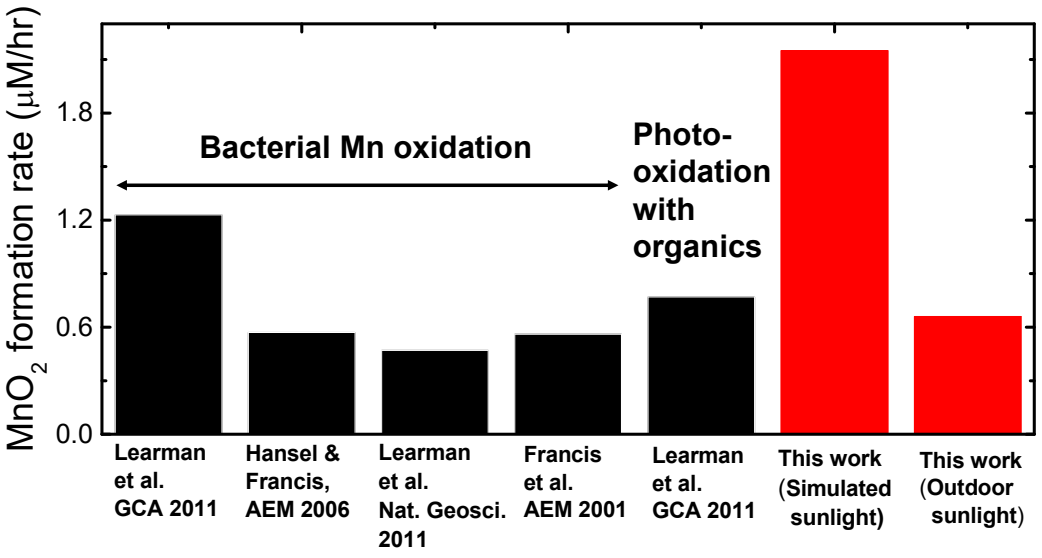

Fig. S9 Comparison of formation rates of MnO_2 in bacteria-mediated systems and in an organic-mediated photooxidation system with that in this work. The bacterially-mediated formation rates of MnO_2 obtained at the end of reaction or reported values from previous results are compared with the formation rates in this study in 1 mM nitrate with sunlight exposure. The comparable formation rates in our preliminary results indicate that photochemically-induced Mn oxidation in nitrate solutions can be a highly possible scenario contributing to δ-MnO_2 formation in the environment.

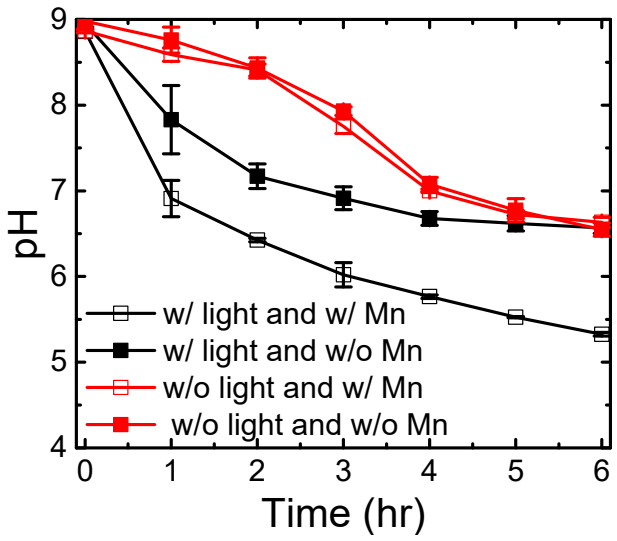

Fig. S10 pH measurement over 6 hrs in photochemically-assisted oxidation of Mn^{2+} (aq) to Mn(IV). The pH decreases without light show the effect of CO_2 absorption over 6 hrs, and are very similar regardless of the existence of Mn^{2+} (aq). Also, the faster decrease of pH under light exposure without Mn^{2+} (aq) shows the effect of nitrate photolysis. Thus, the pH decrease with light and Mn shows the fastest decrease of pH from the effects of Mn^{2+} (aq) oxidation, nitrate photolysis, and CO_2 absorption over 6 hrs.

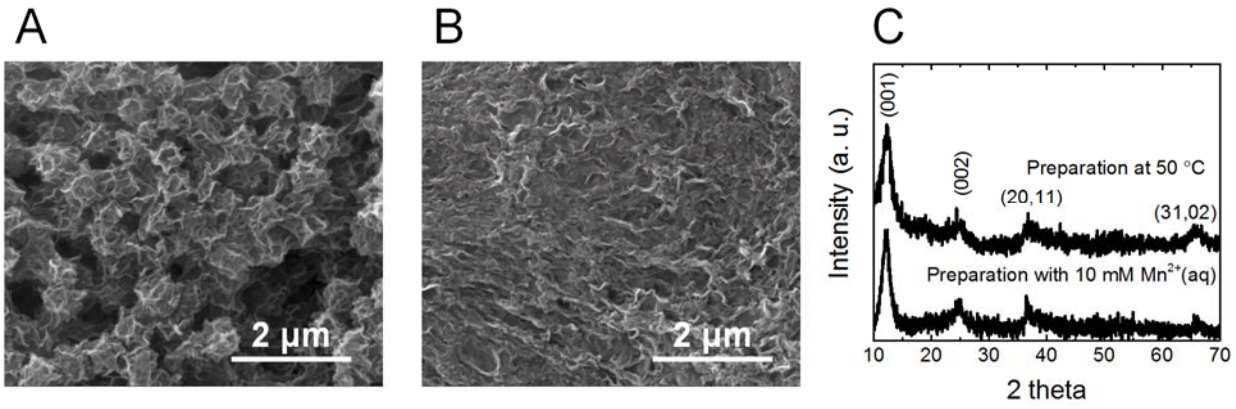

Fig. S11 The formation of δ-MnO_2 nanosheets at 50 °C temperature and 10 mM initial Mn^{2+} (aq) concentration one variable at a time. (A) The morphology of nanosheets formed via the photochemically-assisted pathway at 50 °C. (B) The morphology of nanosheets formed via the photochemically-assisted pathway at 10 mM initial Mn^{2+} (aq). (C) X-ray diffraction patterns identifying the phase of δ-MnO_2 nanosheets synthesized at 50 °C temperature and 10 mM initial Mn^{2+} (aq) concentration one variable at a time.

Supplementary Tables

Table S1. Summary of XPS references for Mn(II), Mn(III), and Mn(IV).

Oxidation state	Mn oxide	Mn $2p_{3/2}$ Binding energy (eV)	ΔE3s	$\Delta E2p_{1/2}$	References
Mn(II)	MnO	640.8	5.8		Junta and Hochella (1994)[11]
	MnO	641.0	6.1		Di Castro and Polzonetti (1989)[40]
	MnO		5.4	6.0	Matsumoto and Sato (1986)[41]
	MnO		6.0	6.0	Gorlin and Jaramillo (2010)[42]
Mn(III)	Mn_2O_3	641.9	5.2		Di Castro and Polzonetti (1989)[40]
	Mn_2O_3	641.8	5.0		Ramesh et al. (2008)[43]
	Mn_2O_3			10.3	Jia Wei et al. (2013)[44]
	Mn_2O_3		5.1	10.0	Gorlin and Jaramillo (2010)[42]
Mn(IV)	MnO_2	642.2	4.7		Oku et al. (1975)[45]
	MnO_2	642.3	4.5		Ramesh et al. (2008)[43]
	MnO_2		4.5	11.8	Gorlin and Jaramillo (2010)[42]
	MnO_2		4.5	11.8	Pinaud et al. (2011)[46]

Table S2. Chemical compositions of the δ-MnO_2 nanosheets. Thermogravimetric analysis (TGA) indicated an approximate 10 wt% decrease by water evaporation at around 200°C, and based on the remaining 90 wt%, the composition was determined as $Mn_{0.92}\square_{0.08}O_2$ (Fig. S3), where □ is vacant sites in the layers, as occurs in δ-MnO_2.

Na/Mn (mol %)	Water percentage (mass %)	Chemical compositions
0.0052 ± 0.0004	10	$Mn_{0.92}\square_{0.08}O_2 \cdot 0.6H_2O$

Table S3. Subsequent reactions during UV photolysis of NO_3^-, adapted from Kim et al. (2014).[7]

UV photolysis of NO_2^- and NO_3^- and production of reactive intermediates		Ref.
$NO^\bullet + NO_2^\bullet + H_2O \rightarrow 2NO_2^- + 2H^+$	(1)	Fischer and Warneck (1996)[47]
$NO^\bullet + NO_3^- \rightarrow NO_2^\bullet + NO_2^-$	(2)	Fischer and Warneck (1996)[47]
$NO_2^\bullet + NO_2^\bullet + H_2O \rightarrow NO_3^- + NO_2^- + 2H^+$	(3)	Fischer and Warneck (1996)[47]
$NO_2^- + h\nu \rightarrow NO_2^{-*}$	(4)	Mack and Bolton (1999)[48]
$NO_2^{-*} \rightarrow NO^\bullet + O^{\bullet-}$	(5)	Mack and Bolton (1999)[48]
$NO_2^{-*} \rightarrow NO_2^\bullet + e_{aq}^-$	(6)	Fischer and Warneck (1996)[47]
$HNO_2 + h\nu \rightarrow NO^\bullet + \bullet OH$	(7)	Fischer and Warneck (1996)[47]
$NO_3^- + h\nu \rightarrow NO_3^{-*}$	(8)	Mack and Bolton (1999)[48]
$NO_3^{-*} \rightarrow NO_2^\bullet + O^{\bullet-}$	(9)	Mack and Bolton (1999)[48]
$NO_2^{-*} \rightarrow NO_2^- + O(^3P)$	(10)	Mack and Bolton (1999)[48]
$O^{\bullet-} + H_2O \leftrightarrow \bullet OH + OH^-$	(11)	Mack and Bolton (1999)[48]
$e_{aq}^- + O_2 \rightarrow O_2^{\bullet-}$	(12)	Buxton et al. (1988)[49]
$2NO^\bullet + O_2 \rightarrow 2NO_2^\bullet$	(13)	Fischer and Warneck (1996)[47]
$\bullet OH + NO_2^- \rightarrow OH^- + NO_2^\bullet$	(14)	Fischer and Warneck (1996)[47]
$\bullet OH + HNO_2 \rightarrow H_2O + NO_2^\bullet$	(15)	Fischer and Warneck (1996)[47]

***** indicates photo-excited species, and • indicates radical species.

Supplementary References

1. B. M. Tebo, B. G. Clement and G. J. Dick, *Manual of Environmental Microbiology*, 2007, **3**, 1223-1238.
2. D. Learman, B. Voelker, A. Vazquez-Rodriguez and C. Hansel, *Nat. Geosci.*, 2011, **4**, 95-98.
3. D. Learman, S. Wankel, S. Webb, N. Martinez, A. Madden and C. Hansel, *Geochim. Cosmochim. Acta*, 2011, **75**, 6048-6063.
4. A. Hammersley, *Inter Rep ESRF98HA01, ESRF, Grenoble*, 1998.
5. Y. Oaki and H. Imai, *Angew. Chem.*, 2007, **119**, 5039-5043.
6. P. Warneck and C. Wurzinger, *J. Phys. Chem.*, 1988, **92**, 6278-6283.
7. D.-H. Kim, J. Lee, J. Ryu, K. Kim and W. Choi, *Environ. Sci. Technol.*, 2014, **48**, 4030-4037.
8. O. C. Zafiriou and M. B. True, *Mar. Chem.*, 1979, **8**, 9-32.
9. D. Diem and W. Stumm, *Geochim. Cosmochim. Acta*, 1984, **48**, 1571-1573.
10. J. J. Morgan, *Geochim. Cosmochim. Acta*, 2005, **69**, 35-48.
11. J. L. Junta and M. F. Hochella Jr, *Geochim. Cosmochim. Acta*, 1994, **58**, 4985-4999.
12. B. Wehrli, G. Friedl and A. Manceau, in *Aquatic Chemistry: Interfacial and Interspecies Processes*, eds. C. P. Huang, C. R. Omelia and J. J. Morgan, American Chemical Society, 1995, vol. 244, pp. 111-134.
13. A. S. Madden and M. F. Hochella, *Geochim. Cosmochim. Acta*, 2005, **69**, 389-398.
14. S. H. Davies and J. J. Morgan, *J. Colloid Interface Sci.*, 1989, **129**, 63-77.
15. R. K. Hocking, R. Brimblecombe, L.-Y. Chang, A. Singh, M. H. Cheah, C. Glover, W. H. Casey and L. Spiccia, *Nat. Chem.*, 2011, **3**, 461-466.
16. W. G. Sunda and S. A. Huntsman, *Mar. Chem.*, 1994, **46**, 133-152.
17. F. F. Marafatto, M. L. Strader, J. Gonzalez-Holguera, A. Schwartzberg, B. Gilbert and J. Peña, *Proc. Natl. Acad. Sci.*, 2015, **112**, 4600-4605.
18. P. S. Nico, C. Anastasio and R. J. Zasoski, *Geochim. Cosmochim. Acta*, 2002, **66**, 4047-4056.
19. D. J. Bertino and R. G. Zepp, *Environ. Sci. Technol.*, 1991, **25**, 1267-1273.
20. K. Kim, H.-I. Yoon and W. Choi, *Environ. Sci. Technol.*, 2012, **46**, 13160-13166.
21. W. G. Sunda, S. A. Huntsman and G. R. Harvey, *Nature*, 1983, **301**, 234-236.
22. W. G. Sunda and D. J. Kieber, *Nature*, 1994, **367**, 62-64.
23. J. P. Lefkowitz, A. A. Rouff and E. J. Elzinga, *Environ. Sci. Technol.*, 2013, **47**, 10364-10371.
24. E. J. Elzinga, *Environ. Sci. Technol.*, 2016, **50**, 8670-8677.
25. H. Zhao, M. Zhu, W. Li, E. J. Elzinga, M. Villalobos, F. Liu, J. Zhang, X. Feng and D. L. Sparks, *Environ. Sci. Technol.*, 2016, **50**, 1750-1758.
26. J. R. Bargar, B. M. Tebo, U. Bergmann, S. M. Webb, P. Glatzel, V. Q. Chiu and M. Villalobos, *Am. Mineral.*, 2005, **90**, 143-154.
27. J. P. Lefkowitz and E. J. Elzinga, *Environ. Sci. Technol.*, 2015, **49**, 4886-4893.
28. B. M. Tebo, H. A. Johnson, J. K. McCarthy and A. S. Templeton, *Trends Microbiol.*, 2005, **13**, 421-428.
29. G. Brouwers, E. Vijgenboom, P. Corstjens, J. De Vrind and E. De Vrind-De Jong, *Geomicrobiol. J.*, 2000, **17**, 1-24.
30. C. A. Francis and B. M. Tebo, *Appl. Environ. Microbiol.*, 2001, **67**, 4272-4278.
31. G.-J. Brouwers, J. P. de Vrind, P. L. Corstjens, P. Cornelis, C. Baysse and E. W. de Vrind-de Jong, *Appl. Environ. Microbiol.*, 1999, **65**, 1762-1768.
32. C. M. Hansel and C. A. Francis, *Appl. Environ. Microbiol.*, 2006, **72**, 3543-3549.
33. C. A. Francis and B. M. Tebo, *Appl. Environ. Microbiol.*, 2001, **67**, 4024-4029.

34. K. Toyoda and B. M. Tebo, *Geochim. Cosmochim. Acta*, 2016, **189**, 58-69.
35. J.-G. Wang, Y. Yang, Z.-H. Huang and F. Kang, *Carbon*, 2013, **61**, 190-199.
36. E. S. Ilton, J. E. Post, P. J. Heaney, F. T. Ling and S. N. Kerisit, *Appl. Surf. Sci.*, 2016, **366**, 475-485.
37. X. Yang, Y. Makita, Z.-h. Liu, K. Sakane and K. Ooi, *Chem. Mater.*, 2004, **16**, 5581-5588.
38. L. Wei, Y.-J. Fan, J.-H. Ma, L.-H. Tao, R.-X. Wang, J.-P. Zhong and H. Wang, *J. Power Sources*, 2013, **238**, 157-164.
39. S. Webb, B. Tebo and J. Bargar, *Am. Mineral.*, 2005, **90**, 1342-1357.
40. V. Di Castro and G. Polzonetti, *J. Electron Spectrosc. Relat. Phenom.*, 1989, **48**, 117-123.
41. Y. Matsumoto and E. Sato, *Mater. Chem. Phys.*, 1986, **14**, 397-426.
42. Y. Gorlin and T. F. Jaramillo, *J. Am. Chem. Soc.*, 2010, **132**, 13612-13614.
43. K. Ramesh, L. Chen, F. Chen, Y. Liu, Z. Wang and Y.-F. Han, *Catal. Today*, 2008, **131**, 477-482.
44. J. W. D. Ng, M. Tang and T. F. Jaramillo, *Energ. Environ. Sci.*, 2014, **7**, 2017-2024.
45. M. Oku, K. Hirokawa and S. Ikeda, *J. Electron Spectrosc. Relat. Phenom.*, 1975, **7**, 465-473.
46. B. A. Pinaud, Z. Chen, D. N. Abram and T. F. Jaramillo, *J. Phys. Chem. C*, 2011, **115**, 11830-11838.
47. M. Fischer and P. Warneck, *J. Phys. Chem.*, 1996, **100**, 18749-18756.
48. J. Mack and J. R. Bolton, *J. Photochem. Photobiol. A: Chem.*, 1999, **128**, 1-13.
49. G. V. Buxton, C. L. Greenstock, W. P. Helman and A. B. Ross, *J. Phys. Chem. Ref. Data*, 1988, **17**, 513-886.